Light extinction and scattering from individual and arrayed high-aspect-ratio trenches in metals

Alexander S. Roberts,[1] Thomas Søndergaard,[2] Manohar Chirumamilla,[2] Anders Pors,[1] Jonas Beermann,[1] Kjeld Pedersen,[2] and Sergey I. Bozhevolnyi[1]

[1]*Centre for Nano Optics, University of Southern Denmark, Campusvej 55, 5230 Odense M, Denmark*

[2]*Department of Physics and Nanotechnology, University of Aalborg, Skjernvej 4, 9220 Aalborg, Denmark*

(Received 23 October 2015; revised manuscript received 15 January 2016; published 4 February 2016)

We investigate the scattering properties of two-dimensional high-aspect-ratio metal trenches acting as resonators for gap-surface plasmons and show that these resonators are highly efficient scatterers of free waves, reaching at resonance in the perfect-conductor limit the unitary dipolar limit for a two-dimensional scatterer. We construct a simple resonator model which predicts the wavelength-dependent extinction, scattering, and absorption cross section of the trench and compare the model findings with full numerical simulations. Both extinction and scattering cross sections are mainly determined by the wavelength and can reach highly supergeometric values. At wavelengths where the metal exhibits near perfect electrical conductor behavior, such trenches lend themselves to be used as self-normalizing scatterers, as their scattering cross section is independent of their geometry and depend only on the resonance wavelength. For real metals with nonzero absorption, efficient monomaterial absorbers and emitters can be fabricated. We extend the analysis to tapering trenches that can be readily fabricated employing common milling or etching techniques and verify by reflection spectroscopy and two-photon luminescence that the resonant behavior of the vertical trenches is preserved.

DOI: 10.1103/PhysRevB.93.075413

I. INTRODUCTION

The study of the coupling between electron gas oscillations inherent to metallic surfaces and freely propagating electromagnetic waves forms the basis of the field of plasmonics, and has led to the investigation of numerous novel applied [1–3] and exploratory concepts [4–7]. Plasmonics has been a highly active research area in recent years, especially since the discovery of extraordinary optical transmission by Ebbesen and co-workers [8]. Optical and infrared absorption, scattering, and transmission of corrugation structures in metallic surfaces has been at the center of attention for many years and continues to be the subject of extensive numerical and experimental research [9,10]. One structure of particular interest is the trench with vertical sidewalls and high aspect ratios, in the sense that its depth greatly exceeds its width. This trend is driven, amongst others, by the emergence of fabricational capabilities allowing for the fabrication of trenches with a high degree of precision and with sizes necessary for resonances in the visible and near infrared. Such capabilities enable the use of gratings of various types for sensing [11–13], thermal emission [14,15], etc. While the mechanism has been elucidated from several angles, the scattering strength of an ideal or perfect metallic slit possesses several characteristics that, under certain circumstances, make it an ideal dipolar scatterer for the scattering of freely propagating waves.

In this work, we investigate a high-aspect-ratio trench in terms of its extinction, scattering, and absorption properties. We present experimental, analytical, and numerical investigations and show that narrow-band absorption stems from the coupling of free-space propagating modes to gap-surface plasmon (GSP) modes propagating in the trench. We develop an analytical model predicting the extinction and scattering cross section on the basis of a GSP mode propagating in the trench and being reflected at the top and bottom terminations, while being excited by an incoming plane-wave field. Resonance occurs due to the Fabry-Perot condition that the round-trip phase accumulation equals an integer multiple of 2π. The developed model shows good correspondence with numerical simulations while being very rapid in terms of computation time, in marked contrast to the full simulations. High-aspect-ratio vertical trenches reach the electric dipolar unitary scattering limit (DUSL) in the perfect-conductor limit at the first-order resonance. For a full theoretical treatment of the maximization of scattering and absorption cross sections, the reader is referred to [16]. Here, we will focus on a vertical trench and a trench with a tapering profile, which is more easily producible employing common milling or etching fabrication techniques.

We thereby build on work by other groups which have previously investigated trenchlike corrugation structures in metals, in either high-aspect-ratio trenches [17,18] or similar configurations [19–23].

II. THEORY

We study a metallic trench with vertical sidewalls, depth d, and width w [Fig. 1(a)] and consider the fundamental GSP mode that can propagate along the trench and reflect at its terminations, forming a simple Fabry-Perot resonator [24].

We assume a strongly subwavelength width $w \ll \lambda_0$, where λ_0 is the vacuum wavelength of the illuminating light. Illumination is at normal incidence by a $\hat{x}$-polarized plane wave of amplitude E_0. This geometry is particularly interesting as it supports one antisymmetric GSP mode (with respect to E_y), for which no cutoff in terms of trench width exists.

A. Gap-surface plasmon single-mode model

1. *Resonator formalism*

Within the trench, GSPs propagate with a propagation constant β and complex-valued reflection coefficients r_b and r_t at the bottom and top terminations, respectively. In the course of one round trip, the plasmon is subjected to both

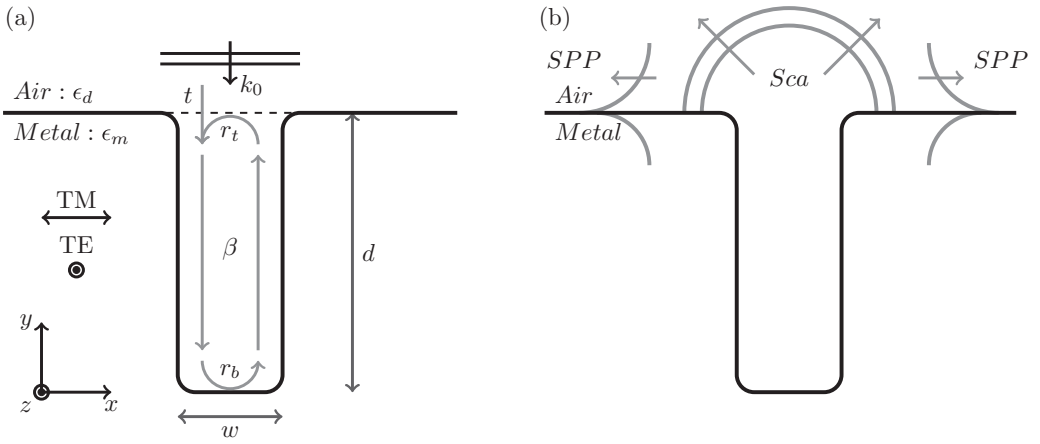

FIG. 1. (a) Schematic of the vertical trench, showing (complex) reflection coefficients and amplitudes as defined in the resonator model. k_0 and β are the wave vectors of the incoming plane wave and the gap-surface plasmon mode supported in the trench, respectively. r_t and r_b are reflection coefficients at the top and bottom terminations, respectively. (b) Definition of the calculated scattering contributions in the GFSI method. The method yields the extinction cross section σ_{ext}, the cross section for scattering to SPPs σ_{SPP}, and the cross section for scattering to plane waves σ_{sca}, of which the two latter are indicated in the schematic.

phase accumulation and amplitude attenuation, described by the complex round-trip modulation τ:

$$\tau \equiv r_b r_t e^{2i\beta d}.$$

In steady state, the amplitude of the downward propagating GSP at the open termination of the trench can be written as an infinite geometric series, due to the summation of an infinite number of contributions with increasing powers of τ:

$$E_d = E_0 t(1 + \tau + \tau^2 + \cdots) = \frac{E_0 t}{1-\tau}. \tag{1}$$

Furthermore, at the open termination, the amplitude of the downward-propagating GSP is related to the two incoming fields, that is, the incoming plane wave and the reflected GSP field, both of which contribute to the downward-propagating amplitude with amplitudes tE_0 and $r_t E_u$, respectively. E_d is, therefore, related to these fields by

$$E_d = r_t E_u + t E_0. \tag{2}$$

The amplitude of the excited field in the aperture E_x is given by the sum of the up- and down-going partial amplitudes

$$E_x = E_d + E_u = E_d(1 + \tau/r_t). \tag{3}$$

Equation (3) follows directly from use of Eqs. (1) and (2). Further elementary manipulation of these three identities leads to the desired expression for the norm-square of the field enhancement (FE) in the trench Γ given by the squared norm of the ratio of the field amplitude in the trench E_x to the amplitude of the incoming field E_0:

$$\Gamma \equiv \left|\frac{E_x}{E_0}\right|^2 = \left|\frac{E_d + E_u}{E_0}\right|^2 = \left|t\frac{1+\tau/r_t}{1-\tau}\right|^2. \tag{4}$$

It can be shown (Appendix A) that the radiated and extincted power (P_{sca} and P_{ext}) by a two-dimensional aperture with a constant electrical field E_x, oriented orthogonally across the gap, is given by

$$P_{\text{sca}} = \frac{k_0 w^2 |E_x|^2}{4\eta_0}, \tag{5a}$$

$$P_{\text{ext}} = \frac{E_0 w}{\eta_0}\text{Re}\{E_x\}, \tag{5b}$$

where $\eta_0 = \sqrt{\mu_0/\epsilon_0}$ is the impedance of free space and w is the width of the trench. Above expressions for the radiated and extincted power enable the calculation of the corresponding cross sections σ_{sca} and σ_{ext}, defined by the ratio of scattered or extincted power to the incident intensity $I = |E_0|^2/2\eta_0$:

$$\sigma_{\text{sca}} = \frac{P_{\text{sca}}}{I} = \frac{k_0 w^2}{2}\left|\frac{E_x}{E_0}\right|^2, \tag{6a}$$

$$\sigma_{\text{ext}} = \frac{P_{\text{ext}}}{I} = 2w\frac{\text{Re}\{E_x\}}{E_0}. \tag{6b}$$

We have now derived the scattering and extinction cross sections, assuming a constant field across the trench opening, in terms of the propagation constant β, transmission and reflection coefficients t, r_b, and r_t, and geometric parameters d and w. The absorption cross section is calculated as $\sigma_{\text{ext}} - \sigma_{\text{sca}}$.

2. *Transmission and reflection coefficients*

The reflection of the downward-propagating GSP mode being reflected at the closed end of the trench is characterized by the fact the GSP mode in the trench has components along the x direction, predominantly. As a consequence, the reflection coefficients can be approximated well by simple Fresnel theory describing the reflection of a plane wave, with appropriate use of mode parameters for the GSP mode. The reflection coefficient is then given by

$$r_b = \frac{1-F}{1+F} \quad \text{with} \tag{7a}$$

$$F = \frac{n_m}{n_{\text{GSP}}} \approx \frac{\sqrt{\varepsilon_m}}{\sqrt{\varepsilon_d + \frac{2\varepsilon_d\sqrt{\varepsilon_d - \varepsilon_m}}{-k_0 w \varepsilon_m}}}, \tag{7b}$$

where n_{GSP} is the effective index for the GSP, for which we use the approximation seen in the denominator of Eq. (7b) [24]. $n_m = \sqrt{\varepsilon_m}$ is the refractive index of the metal, and an air or vacuum gap is assumed with $\varepsilon_d = 1$.

For the reflection at the open termination, we use the reflectivity as derived in Ref. [25] through use of tangential field continuity and energy conservation at the interface:

$$r_t = \frac{1-G}{1+G} \quad \text{with} \tag{8a}$$

$$G = \frac{1}{2\pi} \frac{\int_{-\infty}^{\infty} \frac{k_0}{\eta_0 \sqrt{k_0^2 - k_x^2}} \left[\mathscr{F}\left\{E_x^{\mathrm{tr}}(x,0)\right\}\right]^2 dk_x}{\int_{-\infty}^{\infty} E_x^{\mathrm{tr}}(x,0) H_z^{\mathrm{tr}}(x,0) dx}, \tag{8b}$$

where k_0 and k_x are the scalar values of total and x component of the wave vector, respectively. $\mathscr{F}$ denotes the unitary Fourier transform and $E_x^{\mathrm{tr}}(x,0)$ and $H_z^{\mathrm{tr}}(x,0)$ describe the fields across the open trench termination, which are related as $H_z^{\mathrm{tr}}(x,0) = E_x^{\mathrm{tr}}(x,0)/\eta_0$. The reflection coefficient is calculated for an assumed constant field across the trench and zero field outside, so that $E_x^{\mathrm{tr}}(x,0)$ and $H_z^{\mathrm{tr}}(x,0)$ reduce to rectangular functions.

The transmission coefficient t, governing the transmission of the free-space plane wave to the GSP mode of the trench, is derived in Ref. [26] as

$$t = \left(\frac{2 I_1(0) \sqrt{\frac{\varepsilon_0}{\mu_0}}}{\frac{1}{\lambda}\sqrt{\frac{\varepsilon}{\mu_0}} \int_{-\infty}^{\infty} \frac{|I_1(u)|^2}{\sqrt{1-u^2}} du - \int_{-\infty}^{\infty} E_x^{\mathrm{tr}} H_z^{\mathrm{tr}*} dx} \right)^* \quad \text{with} \tag{9a}$$

$$I_1(u) = \int_{-\infty}^{\infty} E_x^{\mathrm{tr}} e^{-i k_0 u x} dx, \tag{9b}$$

where u denotes spatial frequencies and $*$ denotes the complex conjugate. The approximation of the fields as rectangular functions greatly simplifies the calculations outlined in Eqs. (8b)–(9b).

Without going into details of the derivation of Eq. (9a) given in Ref. [26], it should be mentioned that the implicit assumption of zero field at metal surfaces away from the slit is only strictly valid in the perfect conductor limit. It is thus expected that Eq. (9a) will work best for long wavelengths, at which metals approach the perfect conductor limit.

Equation (6a), in conjunction with Eqs. (7a), (8a), and (9a), constitutes a full, closed description of the scattering power of the trench resonator. As will be shown, this fairly simple model accounts accurately for the extinction and scattering behavior of the resonator, provided that the cross section for scattering into surface plasmon polaritons (SPPs) is small. The fields around the top terminations can excite SPPs propagating away from the trench [27], a behavior not accounted for by the model. Furthermore, evanescent modes inside the resonator can lead to behavior that is unaccounted for in this model. We therefore limit the present considerations to trenches that are deep enough to ensure that the evanescent modes at the terminations do not couple significantly, that is, $d \gg w$.

B. Unitary scattering limits in two and three dimensions

1. Unitary scattering limit in three dimensions

When solving the wave equation in spherical coordinates, the scattering of a sphere can be expressed in terms of the expansion coefficients $|a|$ and $|b|$ in the Riccatti-Bessel basis as [28]

$$\sigma_{\mathrm{sca}} = \frac{2\pi}{k^2} \sum_{n=1}^{\infty} (2n+1)(|a_n|^2 + |b_n|^2), \tag{10}$$

where a_n and b_n are coefficients for expansion into Riccati-Bessel functions of the first (a_n) and second (b_n) kinds of order n. The outgoing dipolar field is represented by coefficient a_1, so in an electric dipolar scattering event, only coefficient a_1 representing an outgoing wave can be nonzero. In the limit of $a_1 \to 1$, one obtains the dipolar unitary scattering limit describing a scattering event in which the scattered power is entirely scattered into the dipolar channel [29]

$$\sigma_{\mathrm{sca}}^{\mathrm{unitary}} = \frac{3}{2} \frac{\lambda^2}{\pi}. \tag{11}$$

Equation (11) is thus the unitary scattering cross section for a dipolar scatterer in three dimensions.

2. Unitary scattering limits in two dimensions

A corresponding expression suitable for describing the unitary, dipolar scattering event in two dimensions can be derived by considering the multipole expansion of the scattering cross section in a cylindrical geometry. In this case, two types of polarizations exist, transverse electric (TE) and transverse magnetic (TM). The scattering cross sections for TE and TM incident light may be formulated in terms of expansion coefficients into cylindrical harmonics, as outlined in [28]. Here, we are only interested in the TM case:

$$\sigma_{\mathrm{sca}}^{\mathrm{TM}} = \frac{4}{k} \left[|a_0|^2 + 2 \sum_{n=1}^{\infty} (|a_n|^2 + |b_n|^2) \right], \tag{12}$$

which in the unitary limit gives

$$\sigma_{\mathrm{sca}}^{\mathrm{TM,unitary}} = \frac{4}{\pi} \lambda. \tag{13}$$

This cross section poses the limit for a dipolar, unitary scattering process, thereby providing the maximum scattering cross section for a lossless scatterer that exhibits purely dipolar behavior. It should be noted that this is not a fundamental upper limit on the total scattering cross section, merely the upper limit for the dipolar scattering channel. Scattering contributions from several channels can increase the cross section arbitrarily (see Ref. [30]).

In the absence of all resonator losses apart from reradiation to the far field, the extincted and the scattered power must be identical. This situation is realized for a trench in a perfect electrical conductor (PEC) material (note that a lossless metal with finite $|\varepsilon|$ still supports SPPs capable of transporting energy away from the trench). It follows directly from the equality of the expressions for σ_{sca} and σ_{ext} that the trench, at strict resonance in the PEC limit, scatters with a cross section

exactly at the DUSL:

$$\sigma_{\mathrm{sca,pec}} = \frac{\sigma_{\mathrm{ext,PEC}}^2}{\sigma_{\mathrm{sca,ext}}} = \frac{\left(2w\frac{\mathrm{Re}\{E_x\}}{E_0}\right)^2}{\frac{\pi w^2}{\lambda_0}\left|\frac{E_x}{E_0}\right|^2} = \frac{4}{\pi}\lambda_0. \qquad (14)$$

In the visible regime, losses are unavoidable at room temperatures. However, the trenches retain substantial scattering power, even with losses.

III. METHODS

We employ two different numerical methods for the calculation of the optical properties of a single trench and a one-dimensional trench array, respectively. All optical properties are calculated using linear interpolations on the data in Ref. [31]. The trench under consideration is of depth d, width w [Fig. 2(a)], and, in the periodic case, period p.

A. Numerical methods

We employ Green's function surface integral method (GFSI) to calculate cross sections for total extinction σ_{ext}, scattering to SPPs propagating away from the trench σ_{SPP}, and scattering to freely propagating light σ_{sca} for illumination at normal incidence. The geometry is fully defined in Fig. 2 for both tapered and vertical side walls, while SPP and free-wave scattering contributions are indicated in Fig. 1(b). A corner rounding radius (s_r) of 4 nm is used in all calculations. For details on the GFSI method, the reader is referred to Appendix B and Refs. [32–34]. The total extinction cross section is defined as the power reduction in the specularly reflected beam due to the trench, normalized to the intensity of the incident beam. In the GFSI simulations, since all scattering contributions are taken into account, any energy loss is associated with material absorption in the trench. As calculations are performed in two dimensions, the validity of the obtained results is limited to cases in which the trench dimension in the z direction is infinite or very large compared to other trench dimensions. We investigate the structure in transverse magnetic (TM) and transverse-electric polarization (TE) with the incident wave vector being antiparallel with the y axis (Fig. 1).

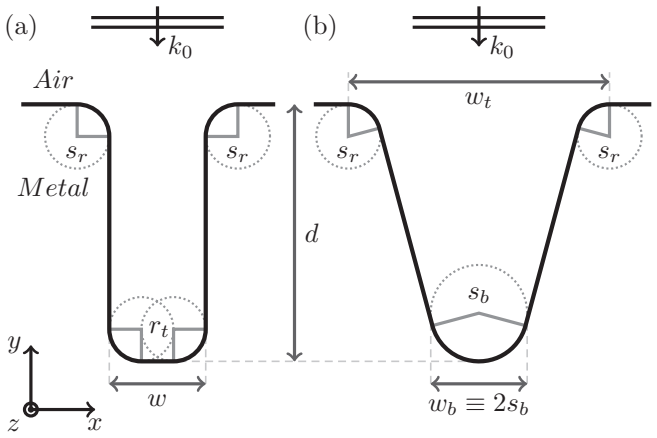

FIG. 2. Definition of the geometry of the vertical trench (a) and tapered trench (b) considered in the numerical calculations. Both vertical and tapering trenches consist entirely of circular sectors and tangentially connected lines. Rounding radii s_r are unchanged at 4 nm. Rotations around z and x define angles θ and ϕ, respectively.

For investigations of arrays of trenches, we implement finite-element simulations in the numerical simulations software COMSOL. The trench geometry is identical to the GFSI simulations, however, with exact plane-wave excitation and Floquet-periodic boundary condition in the x direction. Diffraction orders are handled with additional ports, allowing for the simulation of angled incidence at arbitrary periodicity.

Perfectly periodic arrays of trenches may in some cases support spoof plasmons [35,36], but these cannot be excited by illuminating the surface with a source placed at far-field distances from the surface, which is similar to ordinary SPPs at flat metal surfaces not being excited by such a source. Spoof plasmons are thus not considered here.

B. Fabrication

The investigated trenches are milled into a monocrystalline (100)-gold crystal using focused gallium ion beam milling (FIB). We optimize the tapering trenches for the most vertical side walls while still retaining a nonvanishing radius of curvature at the bottom termination of the trench. Achieving a nonzero width at the bottom termination is crucial to obtain appreciable reflection, i.e., $|r_b| \gg 0$. Conversely, a vanishing radius of curvature will lead to adiabatic focusing of the trench mode, with increasing losses as the plasmon approaches the termination [37]. However, at widths at which the mode is GSP like, the feature sizes approach the resolution of the milling instrument. Hence, the most ideal achievable trenches still divert significantly from vertical walls as convolution with the resolution function and material redeposition alter the desired trench shape and lead to a self-tapering trench profile [38,39]. It should be noted that with the available milling equipment, trenches with such a geometry were not obtainable with smooth side walls. This motivated the use of a gold monocrystal, which is known to be improve the smoothness of FIB-milled structures, as well as increase the scattering intensity of resonant structures [40,41].

C. Experimental methods

1. Reflection spectroscopy

We measure linear reflection spectra of the fabricated samples with an Olympus BX-51 microscope and a 50×-magnifying objective with a numerical aperture of 0.75. Linear reflection spectroscopy on single trenches is performed with an Olympus IX-71 microscope and a 50×-magnifying objective with numerical aperture of 0.5. In both cases we illuminate with a white laser (NKT Photonic, SuperK) at normal incidence. Since this type of laser gives close to circularly polarized light at the power used (roughly 1 W output power), a Glan-Taylor polarizer is used to ensure transverse incident polarization in all discussed measurements. The laser is heavily attenuated with reflective neutral density filters before reaching the microscope to prevent heat damage to the sample and saturation of the fiber-coupled spectrometer. Several spectra taken in succession are used to verify that no observable heat damage is caused. It should be pointed out that the used gold sample is extremely efficient at dissipating heat,

due to its monocrystalline nature and large thickness of 1 mm. Reference spectra are taken on the plane sample surface.

2. Scanning two-photon luminescence microscopy

One well-established experimental technique for the evaluation of field enhancement in nanostructures is two-photon luminescence (TPL) from metals, which was earlier described [42,43] with spatially resolved TPL studies [44,45] and near-field imaging [46] used for characterization of local FEs. We have recently employed diffraction-limited TPL scanning microscopy for direct estimations, and detailed mapping, of FE at the bottom of V grooves [47] and one-dimensional plasmonic black gold [48], both revealing very selective polarization properties of excitation and TPL emission at the narrow groove bottom.

Our experimental setup for TPL microscopy is essentially the same as that described in detail previously [49]. It consists of a scanning optical microscope in reflection geometry built on the base of a commercial microscope and a computer-controlled two-dimensional (2D) piezoelectric translation stage. The linearly polarized light from a mode-locked pulsed (pulse duration 200 fs, repetition rate 80 MHz) Ti:sapphire laser ($\lambda = 740$ nm, $\delta\lambda \approx 10$ nm) is used for sample illumination at the fundamental harmonic (FH) frequency. The illumination power is kept constant at 5 mW and focused with a Mitutoyo infinity-corrected long working distance $\times 100$ objective (N.A. $= 0.7$) at normal incidence. The TPL radiation generated in reflection and the reflected FH beam are collected with the same objective, separated by a wavelength selective beam splitter, directed through appropriate filters and detected with two photomultiplier tubes, the tube for TPL photons being connected with a photon counter obtaining usually less than 10 dark counts per seconds. The integration time for all discussed measurements is 100 ms.

IV. RESULTS

A. Model and numerical results

1. Extinction and scattering of a single trench

Cross-section spectra for total extinction, SPP scattering, and scattering to freely propagating waves for a two-dimensional vertical trench with the geometry defined above [Fig. 2(a)] are obtained using the GFSI method [Figs. 3(a), 3(b), 3(d), and 3(e)]. The considered trench has width $w = 56$ nm and depth $d = 640$ nm. These parameters correspond to those used for trench arrays with a period of

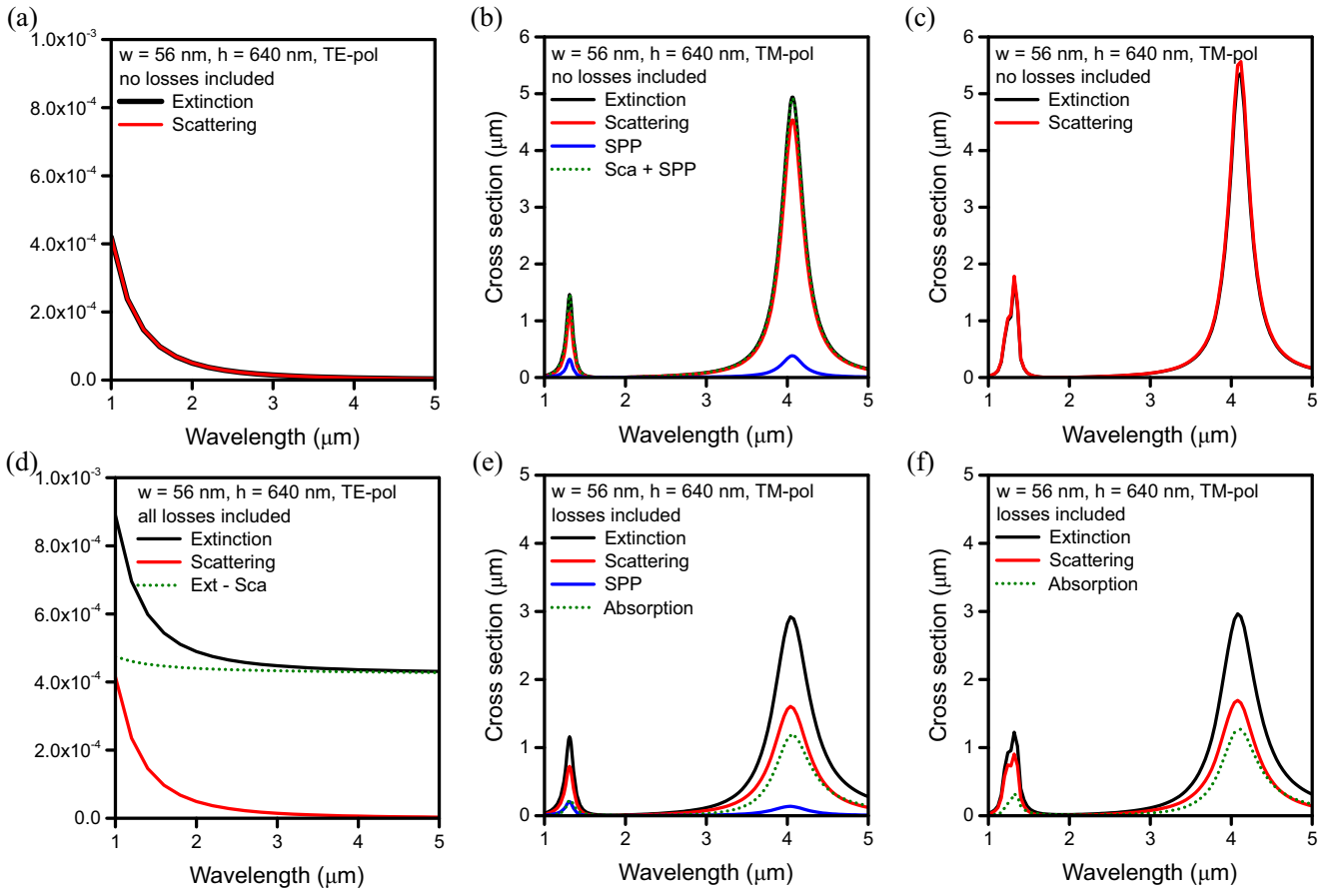

FIG. 3. Comparison between the analytical model and GFSI simulations of an individual trench of width 56 nm and 640 nm depth under normally incident illumination. (a), (d) Show spectra obtained by GFSI simulations for TE-polarized light for omitted and included losses, respectively. (b), (e) Show corresponding spectra for TM polarization while (c) and (f) show spectra obtained by use of the GSP model (for TM polarization). Linear interpolation on the optical data from [31] has been used in all six cases, while neglected losses have been implemented by setting the imaginary part of the dielectric function to zero.

2.472 μm in Ref. [10]. Spectra for TE- and TM-polarized illumination are shown, with and without material losses, respectively. We implement omitted losses by setting the imaginary part of the dielectric constant to zero.

The cross sections for TE-polarized light [Figs. 3(a) and 3(d)] show no resonance and are roughly four orders of magnitude smaller than the corresponding cross sections for TM-polarized light [Figs. 3(b) and 3(e)]. Since TE-polarized light can excite neither propagating SPPs nor modes localized to the resonator, it acts merely as a highly subwavelength, nonresonant surface roughness with correspondingly low cross sections. A slight decrease in the cross section for increasing wavelengths is expected as the disparity between wavelength and trench dimensions becomes larger.

In the lossless case with TM-polarized illumination [Fig. 3(b)], the sum of σ_{SPP} and σ_{sca} is plotted. The correspondence between the total extinction and the sum of scattering and SPP contribution is very good. Since, without Ohmic losses in the metal, there are no other loss channels, this behavior is expected from a physical point of view. Nonetheless, the correspondence indicates a good quality of the partition of the total cross section into parts responsible for scattering into SPPs and out-of-plane propagating waves. It is immediately apparent that σ_{sca} and σ_{ext} have values that exceed the width of the trench substantially (values of 4.4 and 4.9 μm, by factors of 79 and 87, respectively). While the cross section for the excitation of SPP is significantly lower at 0.37 μm, the trench retains a supergeometric cross section of almost 7 w.

The extinction spectra for the lossy trench, under TM-polarized illumination [Fig. 3(e)], show that material losses reduce the scattering cross section to roughly one-third of the DUSL, or $\sigma_{\mathrm{sca}} = 1.6$ μm at a wavelength of 4.04 μm. In other words, the GSP trench is a highly efficient scatterer, with a scattering cross section 28 times larger than its geometrical width. The cross sections for SPP excitation amount to 0.37 μm (lossless) and 0.14 μm (lossy). These results encourage the use of vertical trench scatterers as an alternative to scatterers deposited onto a metallic substrate, providing good geometric scattering enhancements for scattering of plane waves to both surface plasmon polaritons and free waves.

The analytical model is used to calculate extinction, scattering, and absorption cross sections for identical trenches ($w = 56$ nm and $h = 640$ nm), for lossless and lossy gold [Figs. 3(c) and 3(f)]. Considering first the lossless case, it is apparent that, at strict resonance, the scattering cross section exceeds the extinction cross section. This is presumably due to the different sets of approximations on which the calculations of σ_{ext} and σ_{sca} are based (cf. Appendix A). Specifically, the assumption of a point dipole emitter in Eq. (A4) does not enter in the calculation of the extinction cross section. Nonetheless, the model gives very good correspondence in terms of resonance wavelength and satisfactory correspondence in terms of scattering and extinction cross sections at resonance, when compared to GFSI simulations of the same trench [Figs. 3(b) and 3(c)]. It is seen that the model also reliably predicts the second-order resonance of the trench. The asymmetric shape of the second-order resonance around 1.3 μm is due a kink in the optical data [31] to which the model is significantly more sensitive than the GFSI calculation.

When including losses, the correspondence between model and GFSI becomes even more pronounced, and extinction, scattering, and absorption are predicted with high accuracy [Figs. 3(e) and 3(f)]. While this is only possible as long as the SPP cross section is small, it is further facilitated by the fact that the metal at a wavelength of 4 μm behaves close to the PEC limit, which, as pointed out above, enters the model in the form of field-free metals (e.g., in the derivation of t). In the following, we will compare the model predictions to GFSI simulation over a wider range of wavelengths (and material properties) to clarify in which regimes the model is valid.

2. *Model and numerical predictions of scattering of a metallic trench*

In the following, we compare results obtained with the analytical model with GFSI results, focusing on the magnitude of the scattering to clarify the conditions under which one can expect σ_{sca} to approach or reach the DUSL from a vertical trench. While the GFSI method yields the more precise results, the model allows for an investigation of the degree to which an isolated GSP mode is responsible for the scattering predicted.

We calculate a comparison between scattering cross section obtained by the analytical GSP model [Eq. (6a)] and the GFSI method, for 40-nm-wide trenches and depths of 100, 200, 300, 400, 500, and 600 nm, corresponding to resonances ranging from approximately 1 to 4 μm [Fig. 4(a)]. Clearly, the resonance wavelength is well predicted, albeit with an approximate red-shift of 45 nm for all resonances. This

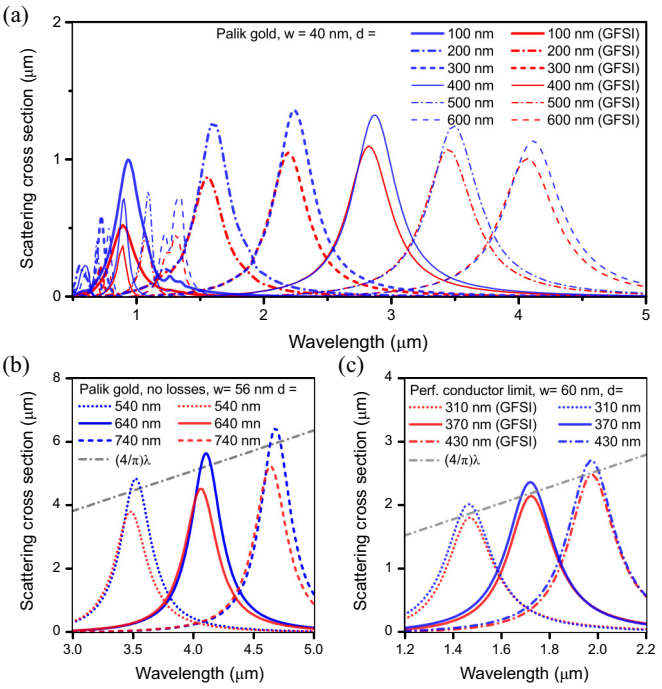

FIG. 4. Comparison between scattering to freely propagating waves spectra obtained from the resonator model (blue curves) and the GFSI method (red curves). (a) Scattering spectra for Palik gold, in the near infrared. (b) Comparison of the unitary scattering limit with scattering spectra obtained for a (Palik) gold trench with neglected losses, i.e., $\mathrm{Im}(\varepsilon) = 0$. (c) Scattering spectra for a trench in the perfect conductor limit $\epsilon \to -\infty$.

behavior is most likely due to the reflection phase of the GSP at the bottom of the trench $\arg(r_b)$ being different from the Fresnel phase by a few percent. The accuracy of the model in terms of the value of the scattering cross section is less pronounced at short wavelengths, where the model increasingly overestimates the scattering cross section σ_{sca}. However, for resonances at longer wavelengths, the correspondence between model and full GFSI simulation is satisfying with a mismatch of only a few percent. This trend can be explained by the fact that the SPP cross section is comparatively large at short wavelengths (not shown). Since SPPs pose an additional loss channel to the resonator, it reduces the amplitude available for scattering to free waves [Eq. (5a)]. Therefore, the field amplitude is overestimated, leading, in turn, to an overestimation of the scattering cross section σ_{sca}. Furthermore, the assumptions for which the transmission t is derived hold poorly at short wavelengths.

For the lossless resonator [Fig. 4(b)], two points are worth noticing. First, the model rather accurately matches GFSI results to within 60 nm in wavelength. Second, despite being less accurate in terms of the size of the scattering cross section, it does correctly predict a strongly scattering trench with a cross section almost two orders of magnitude larger than the width. In fact, the model predicts a cross section slightly above the unitary limit at $4\lambda/\pi$ for all three resonances.

Moving onto the perfect conductor limit ($\varepsilon = -10^9$ is used in the model) for which three resonances are shown in Fig. 4(c), the scattering is predicted by the exact calculations to lie perfectly at the DUSL. Since the effective index of the mode is now equal to one, the resonances are strongly blue-shifted, due to a reduced round-trip phase accumulation. The resonances for the perfect conductor resonator are extremely well reproduced by the GSP model. Since the highly efficient scattering is derived purely from the idealized GSP field at the opening of the trench, one can draw the conclusion that an aperture supporting a GSP mode is an ideal choice for maximizing the dipolar scattering cross section from a resonator.

We now simulate a lossless, vertical trench with metallic properties (ε_m entirely real and negative) approaching the perfect electrical conductor (PEC) limit, to investigate closer the trench behavior in the limit in which no SPPs are launched (Fig. 5). Since a change in the dielectric function leads to a change in the resonance wavelength, the trench depth is adjusted to keep the resonances at (roughly) unchanging wavelengths. For a trench in an $\varepsilon = -10$ material, σ_{SPP} is comparable to the scattering cross section σ_{sca}, amounting to 17 widths, or 680 nm. It is clear that the rise in σ_{sca} with $|\varepsilon|$ is not fully compensated by a corresponding decrease in σ_{SPP} [Figs. 5(a) and 5(c)], wherefore an increased overall extinction is observed [Fig. 5(b)]. Most interestingly, however, the scattering cross section increases to the unitary limit when the metal is near the PEC limit. At resonance ($\lambda_0 = 1620$ nm), the scattering cross section is 2080 nm compared to the DUSL of $4\lambda/\pi = 2070$ nm. Scattering near the DUSL is seen for a dielectric function of $\epsilon = -200$ or greater (in magnitude). This range of dielectric functions is available for gold at wavelengths 2 μm and longer. However, as has been seen in Fig. 4(a), the scattering is also limited by propagation losses of the GSP mode. The introduction of losses leads to a red-shift

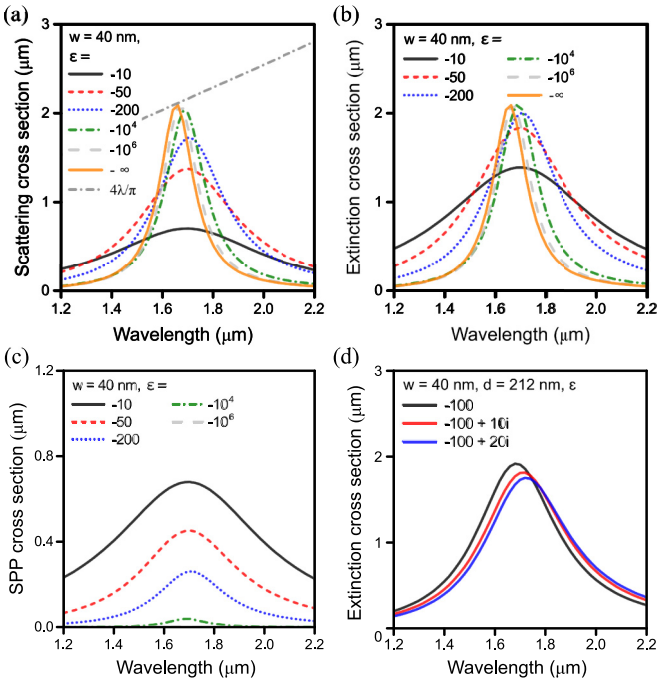

FIG. 5. Cross sections for scattering to (a) freely propagating waves, (b) total extinction, and (c) scattering to SPPs for vertical trenches of width 40 nm, indicated depth h, and ideal metallic properties approaching the perfect electrical conductor limit, i.e., $\epsilon \to -\infty$. The depths of the trenches have been adjusted to keep the resonance roughly stationary and allow for direct comparison. The depths are 84 ($\epsilon = -10$), 178, 246, 350, 370, and 370 nm (PEC) for decreasing dielectric values. In the PEC limit, SPP excitation is suppressed and the scattering cross section reaches the unitary limit. (d) Shows the influence of introduced losses.

and slight broadening of the resonance while lowering the maximum extinction cross section [Fig. 5(d)].

B. Focused ion-beam milled gold trenches

We have fabricated single trenches and arrays of trenches with a period of 600 nm into a monocrystalline gold sample, as described under Methods. Due to the inherently self-tapering profile of narrow FIB-milled features, ideal vertical trenches are not attainable using this procedure. For this reason, the produced trenches have a tapered profile, which we numerically approximate by a linearly tapering geometry [Fig. 2(b)]. The defined trench geometry is comprised of linear and circular sections, merged into a continuous, smooth curve. The trench is thus fully characterized by its top width w_t, a bottom width w_b, and depth d. We investigate eight different trenches (and arrays), all with top width 200 nm and with depths ranging from 200 to 390 nm [Fig. 6(a)].

1. *Extinction analysis*

Reflectance spectra from fabricated trench arrays are measured with TM-polarized illumination at normal incidence [Fig. 6(b)]. The resonances lie at wavelengths from 1.1 to 1.6 μm with a clear red-shift of the resonance with increasing depth and a distinct line shape with nearly linear slopes. It is seen that the strength of the resonance as judged by the dip

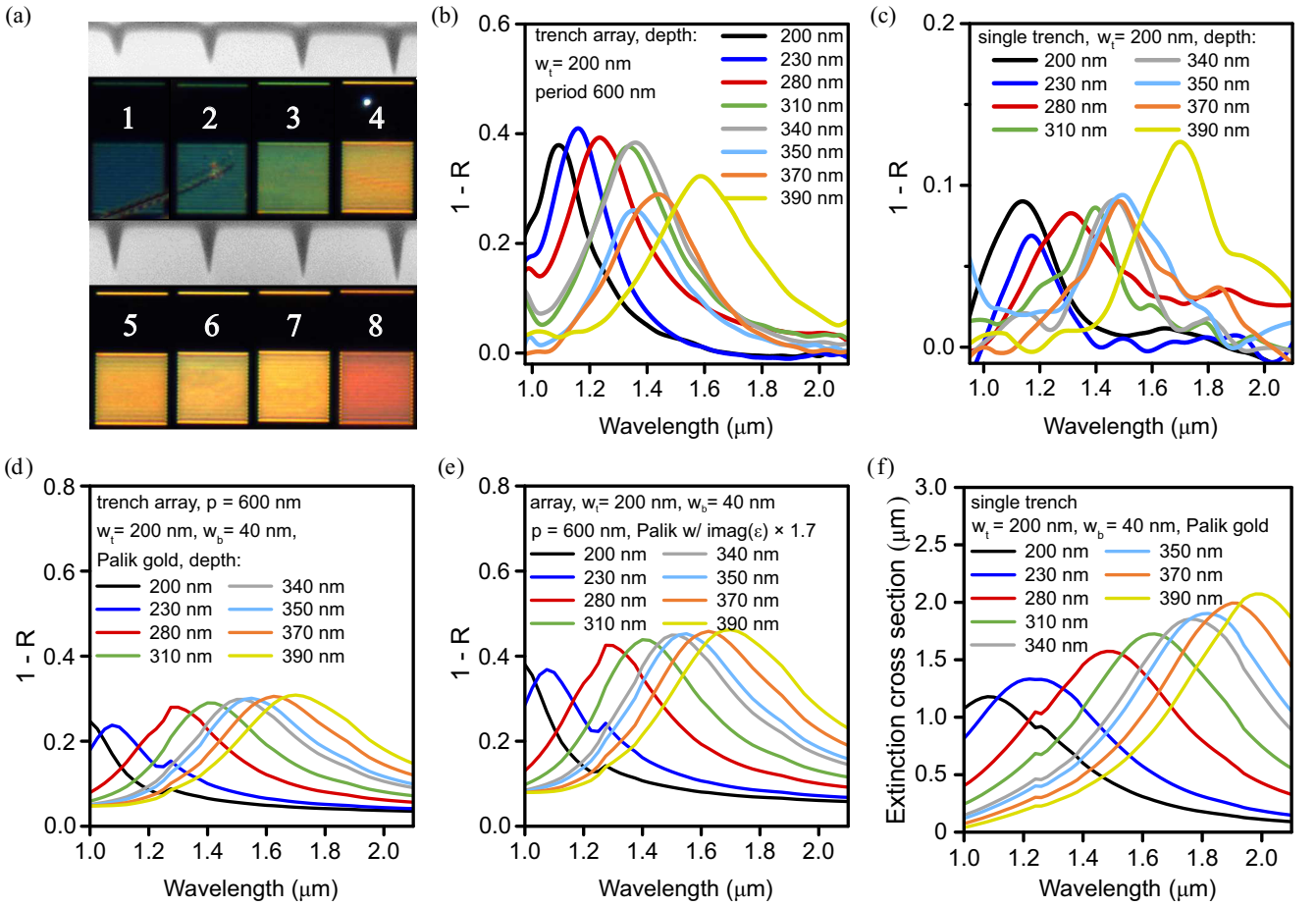

FIG. 6. (a) SEM imaged cross sections of single trenches of increasing depth in a gold monocrystal, obtained by milling away a solid area and dark field microscopy images, showing the scattering of single and arrayed trenches in the visible, due to the second-order resonance. Trench depths: 1: 200 nm, 2: 230 nm, 3: 280 nm, 4: 310 nm, 5: 340 nm, 6: 350 nm, 7: 370 nm, 8: 390 nm. (b) Experimental extinction spectra of first-order resonances of FIB-milled, tapered trench arrays with a top width $w_t = 200$ nm for TM polarization. (c) Experimental single trench extinction spectra for TM polarization. (d) FEM extinction spectra of tapered trenches with $w_t = 200$ nm, $w_b = 40$ nm, and period $p = 600$ nm for a TM-polarized, normal incidence plane wave. (e) FEM simulations of $w_t = 200$ nm, $w_b = 40$ nm, $p = 600$ trench arrays with the imaginary part of the dielectric function increased by a factor of 1.7, leading to an improved agreement with the measured spectra. (f) GFSI simulations of single grooves with $w_t = 200$ nm and $w_b = 40$ nm.

in reflectance (i.e., a peak in *1-R*) decreases with increasing resonance wavelength.

Reflectance measurements of single trenches for TM polarization and a spot size of roughly 3.0 μm are obtained [Fig. 6(c)]. Clear resonances ranging from 1.15 to 1.7 μm are seen for all trench depths and exhibit a red-shift with increasing depth and an accompanying slight increase in the reflectance dip: all trenches cause a reduction in reflection close to 0.1. This is in contrast to the tendency seen for trench arrays where the reflectance dip decreases with increasing wavelength. Finally, comparing single and arrayed trenches, the resonance wavelength of trench arrays is blue-shifted compared to the single trenches of corresponding depths. It should be noted that the measured reflectance cannot be related exclusively to either absorption or extinction cross section. This can be understood by considering the definitions of extinction cross section (power removed from specular reflection of plane wave, normalized to incident power) and absorption cross section (scattered power for incident plane wave normalized to incident power). It is clear from our measurements with intermediate numerical apertures (0.7 and 0.9) that neither of these conditions are fulfilled.

Using FEM simulation, we calculate reflectance spectra for periodic trench arrays with geometrical parameters corresponding to the parameters measured from the SEM scans [Fig. 6(a)] and an array period of $p = 600$ nm for gold with optical properties as described by Palik [Fig. 6(d)], and with the imaginary part of the dielectric function increased by a factor of 1.7. While the use of a gold monocrystal eliminates conduction losses associated with grain boundaries, due to the FIB-milling process, damage occurs to the gold lattice, in addition to Ga^+-ion implantation. Moreover, the presence of the surface inherently increases the electron scattering rate beyond the bulk rate. Both effects increase the optical losses of the gold comprising the trench resonators. We aim to take these effects into account by increasing the imaginary part of the gold permittivity until the best correspondence is reached. This is the case for a factor of 1.7 [Fig. 6(e)]. For thermally evaporated gold, where the scattering on grain boundaries additionally is of importance, values of 3–4 yield

good correspondence [50–52]. It is worth noticing that the observed Q factor of the trenches is actually higher than predicted, which could indicate differences between real and assumed tapering geometries.

Extinction cross-section spectra of single tapered trenches with the measured depths and with the geometry indicated in Fig. 2(b) are calculated using the GFSI method [Fig. 6(f)]. Compared to vertical trenches, the extinction cross section at resonance is reduced by the tapering profile, as well as being subject to considerable broadening. These changes are expected since the GSP mode is reflected less efficiently by a wider top termination, leading to a lower Q factor and, thereby, a broader resonance. The extinction cross section scales almost one-to-one with the wavelength.

The resonance wavelength of the simulations for arrayed trenches shows reasonable correspondence with measurements, for both simulations with altered and unaltered Palik gold. However, this correspondence does not apply for the strength of the reflectance dip, with opposite trends emerging for simulation and measurement. Nonetheless, the overall level can be seen to match for simulations in which above-mentioned alterations to take into account increased losses have been included. Comparing simulations of trench arrays and single trenches, it is obvious that the resonance of single trenches is red-shifted when compared to trench arrays. This behavior is also seen clearly in the measurements when comparing trench arrays and single trench resonances [Figs. 6(b) and 6(c)]. The coupling of plasmonic modes with diffraction orders leads to surface-lattice resonances (see Refs. [53–55]) which have asymmetric line shapes with pronounced (and loss-independent) diffraction features.

The resonance wavelength is somewhat sensitive to the array period, even for periods below the wavelength, where diffraction to free-space waves does not take place. We exemplify this by a goldlike metal with decreasing losses for period of 600 nm in Fig. 7(a) and a period of 1000 nm in Fig. 7(b). In the latter case, the trench resonance is seen at 1.7 μm, with diffraction orders appearing at $p = m\lambda$ for integer m at normal incidence. In both cases, the line shapes are asymmetric due to the coupling with the first diffraction order. It is furthermore seen that the resonance red-shifts with increasing period and the trenches in consequence become increasingly isolated and, therefore, closer to their single isolated behavior. Finally, the extinction can be tuned by appropriate choice of periodicity, making unity absorption attainable even for very low single trench losses. However, as is seen in the insets, a larger period gives a stronger angular dependence of the extinction at resonance. A reflectivity color map of the λ-p parameter space shows the full evolution of the spectrum for increasing periods [Fig. 7(c)]. A corresponding plot for a vertical trench [Fig. 7(d)] highlights that the vertical trench array possesses narrower resonances and is influenced to a lesser extent by diffraction coupling.

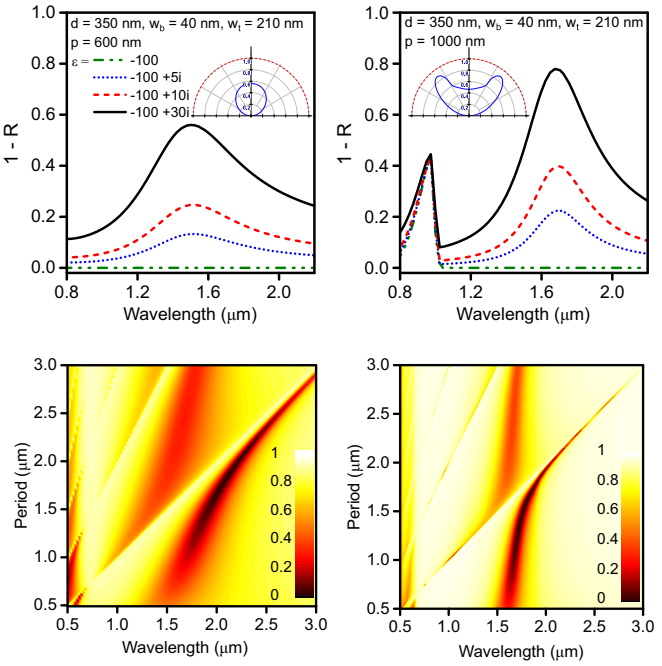

FIG. 7. Spectra of $1 - R$ of tapered trenches with a top width of 210 nm, bottom width 40 nm, and depth 350 nm, indicating the influence of losses at periodicities of (a) 600 nm and (b) 1000 nm. Insets: $1 - R$ dependence on the angle of incidence for in-plane angle for the $\epsilon = -100 + 30i$ material at a wavelength of 1.5 μm. As an aid to the eye, unity is indicated with a red line. (c) Color map of the reflectivity R of tapered trenches for normal incidence, showing the interplay between the plasmonic mode and the diffraction orders at different wavelengths and periods. The trench geometry is identical to (a). (d) Identical to (c), but with a vertical trench of width 40 nm.

2. *TPL analysis*

An indication of the validity of the scattering mechanism outlined in the theory, by which the scattering power is directly related to the intensity enhancement Γ, as indicated by Eq. (5a), can be obtained by measuring the TPL signal from the trenches and observing the degree to which it is proportional to the scattering power. According to previous characterizations of narrow grooves [47,48], the TPL mainly originates from the bottom of the trench where the only emission channel is through GSPs.

Under TM-polarized illumination, the intensity enhancement Γ and scattering power show good correspondence. We interpret this as an indication that tapered trenches, while being resonators of lower quality in terms of Q factors, still retain the scattering mechanism of the vertical trench, where excitation of a single GSP mode leads to reradiation into the far field.

The TPL signal, the intensity enhancement, and the scattering power is obtained at 740 nm, which is the excitation wavelength, or fundamental harmonic (FH), of the TPL measurement (Fig. 8). The intensity enhancement Γ and the field enhancement are calculated by the procedure outlined in [56–58], through the relation

$$\Gamma = \mathrm{FE}^2 = \left(\frac{\mathrm{TPL}_{\mathrm{trench}} \langle \mathrm{P}_{\mathrm{ref}} \rangle^2 A_{\mathrm{ref}}}{\mathrm{TPL}_{\mathrm{ref}} \langle \mathrm{P}_{\mathrm{trench}} \rangle^2 A_{\mathrm{trench}}} \right)^{1/2}, \qquad (15)$$

where TPL is the observed TPL signal, $\langle P \rangle$ is the (time-averaged) illumination power, and A is the area from which the TPL signal stems. While there is certainly some degree of freedom in the choice of A_{trench}, we are interested in observing a common trend between the intensity enhancement Γ and the scattering power divided by the wavelength, as opposed

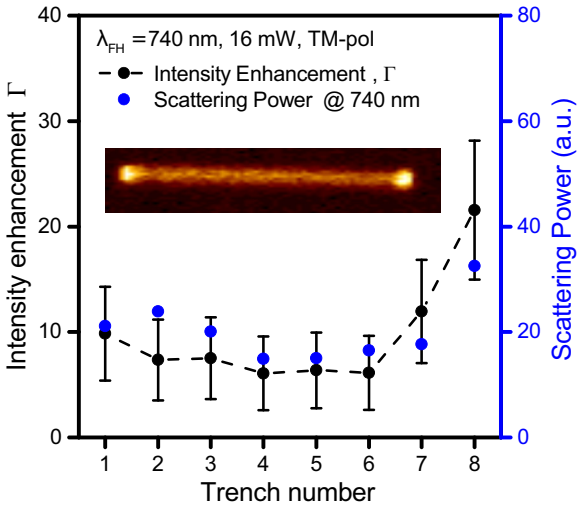

FIG. 8. Intensity enhancement (black dots), calculated from TPL enhancements [Eq. (15)] for an assumed width of 100 nm, and dark-field signal at 740 nm (blue circles). As predicted by the simple model, field enhancement and scattering power follow the same trend. Inset: TPL image of a $14 \times 3\ \mu\text{m}^2$ area containing trench 1. (Trench depths: 1: 200 nm, 2: 230 nm, 3: 280 nm, 4: 310 nm, 5: 340 nm, 6: 350 nm, 7: 370 nm, 8: 390 nm.)

to the numerical value of Γ. We estimate that the TPL stems from a 100-nm-wide area and that the beam is tightly focused. A typical TPL image obtained for the 200-nm-deep trench is seen in the inset of Fig. 8. All the TPL images of the different depths obtained at 740 nm appear similar, but the strength of the TPL signal, the intensity enhancement, and the scattering power significantly depend on the trench depth (Fig. 8).

V. CONCLUSION

In conclusion, we have presented a simple resonator model based on gap surface plasmons, which is capable of accurately predicting the extinction, scattering, and absorption cross sections of a high-aspect-ratio metallic trench. A Green's function surface integral method has been presented and used to verify the model findings and identify that mainly SPP excitation at short wavelength is the main reason for deviation from rigorous theory. We have shown that such trenches can exhibit scattering and extinction cross section that are highly supergeometric and that the two-dimensional unitary scattering limit is reached for metals near the perfect conductor limit. The possibility of highly enhanced extinction cross section encourages the utilization of trench arrays for strong, wavelength selective absorption or thermal emission from a metallic surface. We expand the considerations to tapering trench geometries that are more easily attainable with widespread FIB equipment and fabricate such tapered trenches into a monocrystalline gold substrate. It is verified by reflection spectroscopy that strong resonances exist in tapered trenches and we show, by two-photon luminescence measurements, that tapered trenches exhibit strong field enhancements. Strongly supergeometric cross sections are numerically shown to exist for these trenches. The influence of increasing losses and periodicity is investigated by numerical simulations.

ACKNOWLEDGMENT

We acknowledge financial support from the Danish Council for Independent Research (the FTP project PlasTPV, Contract No. 1335-00104).

APPENDIX A: RADIATION FROM A ONE-DIMENSIONAL APERTURE

In this appendix, we derive expressions for the power extincted and scattered by a subwavelength-wide trench in a PEC film. In principle, these two quantities are equivalent for the PEC case, but for real metals, featuring a complex permittivity with a large negative real part, the extinction also includes the power lost to Ohmic heating. The configuration is depicted in Fig. 1, with the incident light propagating along the $-y$ axis and being TM polarized. The metal interface is assumed to be at $y = 0$, while the surrounding medium is chosen to be air. It is evident that for $w \ll \lambda$ and far away from any trench resonance, the electromagnetic field in the upper half-space can be approximated by the incident and specularly reflected wave, hereby giving rise to the standing-wave pattern

$$E_x^{(+)} = -2i\,E_0 \sin(k_0 y), \quad H_z^{(+)} = 2E_0/\eta_0 \cos(k_0 y), \quad \text{(A1)}$$

where E_0 is a real-valued positive constant representing the amplitude of the incident wave, k_0 is the free-space wave number, and η_0 is the vacuum impedance. We note that it is the above field that can be considered as the driving field when exciting trench resonances. Moreover, it is clear that $E_x^{(+)} = 0$ and $H_z^{(+)} = 2E_0/\eta_0$ at the metal boundary ($y = 0$). Since extinction is related to the interference between the driving and scattered fields, the power extincted by the trench can, in general, be written as [28]

$$P_{\text{ext}} = -\frac{1}{2}\int_{-w/2}^{w/2} \text{Re}\{\mathbf{E}^{(+)} \times \mathbf{H}^{\text{sc},*} + \mathbf{E}^{\text{sc}} \times \mathbf{H}^{(+),*}\} \cdot \hat{\mathbf{y}}\, dx, \quad \text{(A2)}$$

where $(\mathbf{E}^{\text{sc}}, \mathbf{H}^{\text{sc}})$ are the scattered fields evaluated at the trench aperture, and $*$ means complex conjugate. The above expression can be easily simplified, yielding

$$P_{\text{ext}} = \frac{E_0 w}{\eta_0} \text{Re}\{\langle E_x \rangle\}. \quad \text{(A3)}$$

Here, $\langle \ldots \rangle$ means average value, and we have used the fact that the total electric field at the trench aperture $E_x = E_x^{\text{sc}}$. It should be noted that in the resonator model presented in the main text, E_x is assumed constant across the aperture and, hence, also represents the average value. Furthermore, it is important to realize that Eq. (A3) implies that $\text{Re}\{\langle E_x \rangle\}$ is always positive. The physical origin of this property derives from the fact that light scattered from any resonator changes from being in phase to out of phase with the driving field as one crosses the resonance from the low-frequency side. As Eq. (A1) represents the driving field for the trench, it naturally follows that the phase of the electric field changes from $-\pi/2$ to $\pi/2$ when crossing the resonance from the low-frequency side, thus entailing that $\langle E_x \rangle$ is purely real at the resonance and $\text{Re}\{\langle E_x \rangle\} \geqslant 0$ at any wavelength.

In the remainder of the appendix, we calculate the power scattered by the trench. From the field equivalence principle

and image theory, it is possible to show that radiation from an aperture in a PEC film corresponds to radiation of a magnetic surface current defined by [59]

$$\mathbf{J}_m = -2(\hat{\mathbf{n}}_a \times \mathbf{E}_a), \tag{A4}$$

where $\mathbf{E}_a$ is the electric field in the plane of the aperture and $\hat{\mathbf{n}}_a$ is the surface normal. In this work, the scattering from the subwavelength trench can in the far-field zone be approximated by the radiation from the point source

$$\mathbf{J}_m = 2\langle E_x \rangle w \hat{\mathbf{z}}, \tag{A5}$$

which is assumed to be positioned at the center of the coordinate system. The associated far-field magnetic vector potential is given by

$$\mathbf{A}_m^{\text{far}}(\mathbf{r}) = \varepsilon_0 \mathbf{J}_m g_0^{\text{far}}(\mathbf{r},0), \tag{A6}$$

where

$$g_0^{\text{far}}(\mathbf{r},0) = \frac{i}{\sqrt{8\pi k_0 r}} e^{i(k_0 r - \pi/4)} \tag{A7}$$

is the asymptotic expression of the free-space Green's function for large arguments, ε_0 is the free-space permittivity, $\mathbf{r} = x\hat{\mathbf{x}} + y\hat{\mathbf{y}}$ is the position vector in the xy plane, and $r = |\mathbf{r}|$. The electric far field is defined by $\mathbf{E}^{\text{far}} = -ik_0/\varepsilon_0(\hat{\mathbf{r}} \times \mathbf{A}_m^{\text{far}})$, corresponding to

$$\mathbf{E}^{\text{far}}(\mathbf{r}) = -\frac{w\sqrt{k_0}\langle E_x \rangle}{\sqrt{2\pi r}} e^{i(k_0 r - \pi/4)} \hat{\varphi}, \tag{A8}$$

where $\hat{\varphi} = \hat{\mathbf{z}} \times \hat{\mathbf{r}}$. As the far field from any current source locally behaves as a plane wave, the time-averaged Poynting vector in the direction $\hat{\mathbf{r}}$ can be written as $\mathbf{S}^{\text{far}} = \frac{1}{2\eta_0}|\mathbf{E}^{\text{far}}|^2 \hat{\mathbf{r}}$. The total power radiated into the upper half-space can now be found by direct integration of the power flowing through the circular line segments $r d\theta$, i.e.,

$$P_{\text{sc}} = \int_0^{\pi} \mathbf{S}^{\text{far}} \cdot \hat{\mathbf{r}}\, r d\theta = \frac{k_0 w^2}{4\eta_0} |\langle E_x \rangle|^2. \tag{A9}$$

APPENDIX B: CALCULATION OF EXTINCTION FROM A SINGLE TRENCH IN A METAL SURFACE

In this appendix, we will present briefly the integral equation method used in this paper to calculate scattering from a single trench in a metal surface. In this method, the field at all positions is related to the field and its normal derivative at the surface of a scattering object through integral equations. It is sufficient to reduce the numerical problem at first to only the surface of the scattering object, and the radiating boundary condition is automatically taken care of via the choice of Green's function.

We will describe the structure following the procedure shown in Fig. 9. Here, a region shaped as the trench (the scattering object) is buried inside the metal of a two-layer air-metal reference geometry. In the limit where the trench-shaped region is moved upwards until it touches the air-metal interface ($\delta \to 0$), the resulting structure is a trench in an air-metal surface.

We will assume that the incident light is p polarized and propagating in the xy plane, and the magnetic field will thus

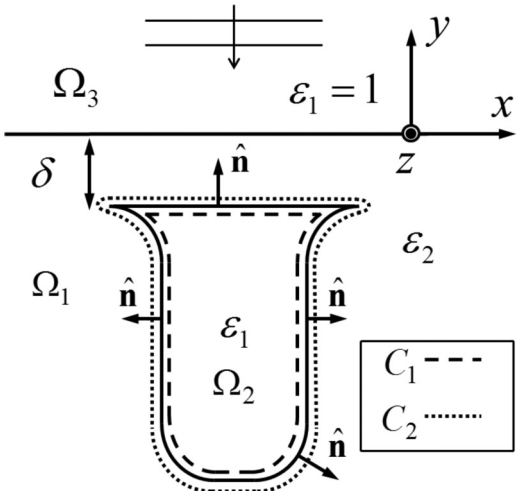

FIG. 9. Schematic of obtaining a trench in a metal surface by adding an air scatterer in the metal region, and then taking the limit of moving the scatterer upwards ($\delta \to 0$) until it is no longer buried inside the metal.

be of the form

$$\mathbf{H}(\mathbf{r}) = \hat{\mathbf{z}} H(\mathbf{r}), \tag{B1}$$

where $\mathbf{r} = \hat{\mathbf{x}}x + \hat{\mathbf{y}}y$ is a position in the xy plane.

The field at any position inside the trench (Ω_2 in Fig. 9) can be expressed in terms of the field and its normal derivative at the boundary C_1 (see Fig. 9) by the following surface integral equation [60]:

$$H(\mathbf{r}) = \int_{C_1} \left\{ g_2(\mathbf{r},\mathbf{r}') \hat{\mathbf{n}}' \cdot \nabla' H(\mathbf{r}') - H(\mathbf{r}') \hat{\mathbf{n}}' \cdot \nabla' g_2(\mathbf{r},\mathbf{r}') \right\} dl', \tag{B2}$$

where $\hat{\mathbf{n}}$ is the outward normal vector (see Fig. 9), and g_2 can be chosen as the free-space Green's function

$$g_2(\mathbf{r},\mathbf{r}') = \frac{i}{4} H_0^{(1)}(k_0 n_1 |\mathbf{r} - \mathbf{r}'|). \tag{B3}$$

Here, k_0 is the free-space wave number, n_1 is the refractive index inside the trench ($n_1 = 1$), and $H_0^{(1)}$ is the Hankel function of zero order and first kind.

For positions outside the trench (Ω_1 and Ω_3), the field must be described as the sum of the reference field, which is a solution for the case where the trench is absent, and field components propagating away from the trench. This can be expressed by the integral equation

$$H(\mathbf{r}) = H_{\text{ref}}(\mathbf{r}) - \int_{C_2} \{ g_1(\mathbf{r},\mathbf{r}') \hat{\mathbf{n}}' \cdot \nabla' H(\mathbf{r}') - H(\mathbf{r}') \hat{\mathbf{n}}' \cdot \nabla' g_1(\mathbf{r},\mathbf{r}') \} dl'. \tag{B4}$$

Two cases must be considered for the air-metal reference structure Green's function g_1. If both $y < 0$ and $y' < 0$, then

$$g_1(\mathbf{r},\mathbf{r}') = \frac{i}{2\pi} \int_{\kappa_x = 0}^{\infty} \frac{\cos(\kappa_x [x - x'])}{\kappa_{y2}} \times \frac{\left(e^{i\kappa_{y2}|y-y'|} + r_{13}^{(p)}(\kappa_x) e^{-i\kappa_{y2}(y+y')} \right)}{\kappa_{y2}} d\kappa_x, \tag{B5}$$

where the reflection coefficient is given by

$$r_{13}^{(p)}(\kappa_x) = \frac{\varepsilon_1\kappa_{y2} - \varepsilon_2\kappa_{y1}}{\varepsilon_1\kappa_{y2} + \varepsilon_2\kappa_{y1}}, \tag{B6}$$

with $\kappa_{yi} = \sqrt{k_0^2\varepsilon_i - \kappa_x^2}$ and $\mathrm{Im}\{\kappa_{yi}\} \geqslant 0$. On the other hand, if $y' < 0$ and $y > 0$, then

$$g_1(\mathbf{r},\mathbf{r}') = \frac{i}{2\pi}\int_{\kappa_x=0}^{\infty} \frac{\cos(\kappa_x[x-x'])e^{-i\kappa_{y2}y'+i\kappa_{y1}y}t_{13}^{(p)}(\kappa_x)}{\kappa_{y2}}d\kappa_x, \tag{B7}$$

where the transmission coefficient is given by

$$t_{13}^{(p)}(k_x) = 1 + r_{13}^{(p)}(k_x). \tag{B8}$$

For calculating the field and normal derivative at the boundary C_1 we only need Eq. (B5).

For the reference structure magnetic field entering the integral equation we choose the solution for the reference geometry in the case of a normally incident plane wave:

$$H_{\mathrm{ref}}(\mathbf{r}) = H_i\begin{cases} e^{-ik_0n_1y} + r_{31}^{(p)}(\kappa_x=0)e^{+ik_0n_1y}, & y > 0 \\ t_{31}^{(p)}(\kappa_x=0)e^{-ik_0n_2y}, & y < 0. \end{cases} \tag{B9}$$

Here, $r_{31}^{(p)} = -r_{13}^{(p)}$ and $t_{31}^{(p)} = 1 + r_{31}^{(p)}$.

The scatterer surface is now subdivided into small discrete elements on which the field and normal derivative are assumed to vary linearly from one end to the other. The field and its normal derivative at the end of one element can be directly related to their counterpart at the beginning of another neighbor element through boundary conditions, and thus the right-hand sides of Eqs. (B2) and (B4) can be cast in parameters for the beginning of elements only. By now letting $\mathbf{r}$ approach the position of the beginning of an element from either side (Ω_1 or Ω_2) self-consistent equations are obtained for the parameters that can be cast on matrix form. This must, in addition, be combined with boundary conditions relating the field and normal derivative just outside the scatterer boundary with their counterparts just inside the boundary.

After solving the resulting matrix equation, we are now ready to calculate the extinction and scattering cross sections. The scattered field can be obtained using Eq. (B4) and the calculated fields at C_2:

$$H_{\mathrm{scat}}(\mathbf{r}) = -\int_{C_2}\big\{g_1(\mathbf{r},\mathbf{r}')\hat{\mathbf{n}}'\cdot\nabla' H(\mathbf{r}') - H(\mathbf{r}')\hat{\mathbf{n}}'\cdot\nabla' g_1(\mathbf{r},\mathbf{r}')\big\}dl'. \tag{B10}$$

If we now use $\mathbf{r} = \hat{\mathbf{x}}r\cos\theta + \hat{\mathbf{y}}r\sin\theta$ with $\theta \in]0;\pi[$, and consider large distances r ($k_0r \gg 1$), and in principle also large distances to the surface, then we can replace the Green's function (B7) with the corresponding far-field approximation given by [60]

$$g_1^{ff}(\mathbf{r},\mathbf{r}') = \frac{e^{ik_0n_1r}}{\sqrt{r}}e^{i\pi/4}\frac{1}{2}\frac{1}{\sqrt{2\pi}}\frac{1}{\sqrt{k_0n_1}} \times\left[\frac{\kappa_{y1}}{\kappa_{y2}}t_{13}^{(p)}(\kappa_x)e^{-i\kappa_x x'}e^{-i\kappa_{y2}y'}\right], \tag{B11}$$

where here $\kappa_x = k_0n_1\cos\theta$, $\kappa_{y1} = k_0n_1\sin\theta$, and $\kappa_{y2} = \sqrt{k_0^2\varepsilon_2 - \kappa_x^2}$ with $\mathrm{Im}\{\kappa_{y2}\} \geqslant 0$. Note that here κ_x can assume negative values for $\pi/2 < \theta < \pi$. With this expression it is straightforward to evaluate the field at large distances r, and the scattering cross section for scattering into the upper half-plane can now be obtained using

$$\sigma_{\mathrm{scat}} = \lim_{r\to\infty}\frac{1}{|H_i|^2}\int_{\theta=0}^{\pi}|H_{\mathrm{scat}}(r,\theta)|^2 r\,d\theta. \tag{B12}$$

In order to evaluate the extinction cross section, we need only to consider the scattered field for a single direction but all phase information must be maintained. We consider a case of a wide Gaussian beam being incident on the scatterer, where the Gaussian beam width must be so large that the incident field is plane-wave-like. In that case, the power removed from the reflected beam due to the presence of the scatterer can be calculated and will be independent of the width of the incident Gaussian beam. If this power is then normalized by the incident power per unit area of the incident plane wave, we obtain the extinction cross section

$$\sigma_{\mathrm{ext}} = -\frac{2\sqrt{\frac{2\pi}{k_0}}}{|H_i|^2}\mathrm{Re}\big\{r_{31}^{(p)}(\theta=\pi/2)[H_{\mathrm{scat}}(r,\theta=\pi/2)]^* \times\sqrt{r}e^{ik_0r}e^{-i\pi/4}H_i(\mathbf{r}=\mathbf{0})\big\}. \tag{B13}$$

Here, $r^{(p)} = r_{31}^{(p)} = -r_{13}^{(p)}$.

For positions close to the air-metal interface ($y = 0$) it is also relevant to consider the contribution to g_1 from the pole of $t_{13}^{(p)}(\kappa_x)$, which here leads to

$$g_1^{(\mathrm{SPP})}(\mathbf{r},\mathbf{r}') = -\frac{1}{2}e^{i\kappa_{x,\mathrm{SPP}}|x-x'|}e^{-i\kappa_{y2,\mathrm{SPP}}y'}\frac{A}{\kappa_{y2,\mathrm{SPP}}} \times\begin{cases}\exp(i\kappa_{y1,\mathrm{SPP}}y), & y > 0 \\ \exp(-i\kappa_{y2,\mathrm{SPP}}y), & y < 0\end{cases} \tag{B14}$$

where

$$\kappa_{x,\mathrm{SPP}} = k_0\sqrt{\frac{\varepsilon_1\varepsilon_2}{\varepsilon_1+\varepsilon_2}}, \tag{B15}$$

$$A = \lim_{\kappa_x\to\kappa_{x,\mathrm{SPP}}}\left(t_{13}^{(p)}(\kappa_x)(\kappa_x - \kappa_{x,\mathrm{SPP}})\right) = -\frac{2\varepsilon_1\kappa_{y2,\mathrm{SPP}}}{\kappa_{x,\mathrm{SPP}}\left(\frac{\varepsilon_1}{\kappa_{y2,\mathrm{SPP}}} + \frac{\varepsilon_2}{\kappa_{y1,\mathrm{SPP}}}\right)}, \tag{B16}$$

and $\kappa_{yi,\mathrm{SPP}} = \sqrt{k_0^2\varepsilon_i - \kappa_{x,\mathrm{SPP}}^2}$ with $\mathrm{Im}\{\kappa_{yi,\mathrm{SPP}}\} \geqslant 0$.

The excitation of the SPP left- and right-propagating guided modes can then be calculated by inserting $g_1^{(\mathrm{SPP})}$ into Eq. (B10). For a position x located to the right of the trench ($x > x'$ for all relevant x' of the curve C_2), we find

$$H_{\mathrm{SPP}}(\mathbf{r}) = H_{\mathrm{SPP},0}e^{i\kappa_{x,\mathrm{SPP}}x}\begin{cases}\exp(i\kappa_{y1,\mathrm{SPP}}y), & y > 0 \\ \exp(-i\kappa_{y2,\mathrm{SPP}}y), & y < 0\end{cases} \tag{B17}$$

where

$$H_{\mathrm{SPP},0} = \frac{\varepsilon_1\kappa_{y1,\mathrm{SPP}}\kappa_{y2,\mathrm{SPP}}}{\kappa_{x,\mathrm{SPP}}(\varepsilon_1\kappa_{y,\mathrm{SPP}} + \varepsilon_2\kappa_{y2,\mathrm{SPP}})}\int_{C_2}e^{-i\kappa_{x,\mathrm{SPP}}x'}e^{-i\kappa_{y2,\mathrm{SPP}}y'} \times[\hat{\mathbf{n}}'\cdot\nabla' H(\mathbf{r}') - H(\mathbf{r}')\hat{\mathbf{n}}'\cdot(\hat{\mathbf{x}}(-i\kappa_{x,\mathrm{SPP}}) + \hat{\mathbf{y}}(-i\kappa_{y2,\mathrm{SPP}}))]dl'. \tag{B18}$$

A similar expression can be obtained for the left-propagating SPP ($x < x'$). In the case of normally incident light, it is sufficient to consider the power carried by the right-propagating SPP and then multiplying by a factor of 2 to obtain the total power scattered into SPP waves. Scattering into guided modes of a geometry supporting many guided modes was recently considered in [61].

The total time-averaged power carried by the right-propagating SPP wave at a given x is given by

$$P_{\mathrm{SPP},r} = \frac{1}{2}\mathrm{Re}\int_y \{\mathbf{E}^{(\mathrm{SPP})}(\mathbf{r}) \times (\mathbf{H}^{(\mathrm{SPP})}(\mathbf{r}))^* \cdot \hat{\mathbf{x}}\} dy. \quad \text{(B19)}$$

By normalizing with the incident power per unit area and rewriting in terms of the magnetic field only, we find the scattering cross section related to the excitation of right-propagating SPP waves

$$\sigma_{\mathrm{SPP},r} = \frac{|H_{\mathrm{SPP},0}|^2}{|H_i|^2} e^{-2\kappa_{x,\mathrm{SPP},i}x}\left(\mathrm{Re}\left\{\frac{\kappa_{x,\mathrm{SPP}}}{k_0 n_1}\right\}\frac{1}{2\kappa_{y1,\mathrm{SPP},i}} + \mathrm{Re}\left\{\frac{\kappa_{x,\mathrm{SPP}}}{k_0 n_1}\frac{\varepsilon_1}{\varepsilon_2}\right\}\frac{1}{2\kappa_{y2,\mathrm{SPP},i}}\right), \quad \text{(B20)}$$

where $\kappa_{x,\mathrm{SPP},i} = \mathrm{Im}\{\kappa_{x,\mathrm{SPP}}\}$, and $\kappa_{yi,\mathrm{SPP},i} = \mathrm{Im}\{\kappa_{yi,\mathrm{SPP}}\}$.

It should be noted that in the case of no absorption losses then $\sigma_{\mathrm{ext}} = \sigma_{\mathrm{scat}} + \sigma_{\mathrm{SPP},r} + \sigma_{\mathrm{SPP},l}$ identically, where $\sigma_{\mathrm{SPP},l}$ is the cross section related to left-propagating SPP waves, while in the case of absorption losses we expect $\sigma_{\mathrm{ext}} > \sigma_{\mathrm{scat}} + \sigma_{\mathrm{SPP},r} + \sigma_{\mathrm{SPP},l}$ due to excess absorption losses related to the trench. The case of absorption losses is tricky though since clearly the SPP scattering cross sections depend on the value of x where the SPP field is evaluated.

We have also considered scattering for s-polarized light. In that case, the calculations were done by replacing in the above expressions the magnetic field H with the electric field E, and replacing Fresnel reflection and transmission coefficients with their s-polarized counterparts. In this case, the Green's function g_1 is then different, and also the boundary condition relating the normal derivative of the field on one and the other side of the scatterer surface is different. Note that for s polarization, the air-metal geometry does not support guided modes, and also the Fresnel reflection and transmission coefficients no longer have a pole. Thus, no scattering of light into guided modes should be considered for this polarization (for this particular geometry).

[1] W. Turner *et al.*, Trends Ecol. Evol. **18**, 306 (2003).
[2] A. Kabashin *et al.*, Nat. Mater. **8**, 867 (2009).
[3] N. Liu, M. Mesch, T. Weiss, M. Hentschel, and H. Giessen, Nano Lett. **10**, 2342 (2010).
[4] S. V. Yalunin, M. Gulde, and C. Ropers, Phys. Rev. B **84**, 195426 (2011).
[5] X. Ni, N. Emani, A. Kildishev, A. Boltasseva, and V. Shalaev, Science **335**, 427 (2012).
[6] M. G. G. Herink, D. R. Solli, and C. Ropers, Nature (London) **483**, 190 (2012).
[7] A. Väkeväinen *et al.*, Nano Lett. **14**, 1721 (2013).
[8] T. W. Ebbesen, H. Lezec, H. Ghaemi, T. Thio, and P. Wolff, Nature (London) **391**, 667 (1998).
[9] F. J. Garcia-Vidal, L. Martin-Moreno, T. W. Ebbesen, and L. Kuipers, Rev. Mod. Phys. **82**, 729 (2010).
[10] R. H. F. Pardo, P. Bouchon, R. Haider, and J.-L. Pelouard, Phys. Rev. Lett. **107**, 093902 (2011).
[11] S. Lal, S. Link, and N. J. Halas, Nat. Photon. **1**, 641 (2007).
[12] F. Hao *et al.*, Nano Lett. **8**, 3983 (2008).
[13] R. Gordon, D. Sinton, K. L. Kavanagh, and A. G. Brolo, Acc. Chem. Res. **41**, 1049 (2008).
[14] M.-W. Tsai, T.-H. Chuang, C.-Y. Meng, Y.-T. Chang, and S.-C. Lee, Appl. Phys. Lett. **89**, 173116 (2006).
[15] R. Stanley, Nat. Photon. **6**, 409 (2012).
[16] J.-P. Hugonin, M. Besbes, and P. Ben-Abdallah, Phys. Rev. B **91**, 180202 (2015).
[17] A. Polyakov *et al.*, Sci. Rep. **2**, 933 (2012).
[18] S. Kim *et al.*, Opt. Express **21**, 15081 (2013).
[19] A. Polyakov *et al.*, Appl. Phys. Lett. **98**, 203104 (2011).
[20] A. Polyakov *et al.*, J. Vac. Sci. Technol. B **29**, 06FF01 (2011).
[21] L. Meng, D. Zhao, Q. Li, and M. Qiu, Opt. Express **21**, A111 (2013).
[22] J. Le Perchec, P. Quemerais, A. Barbara, and T. Lopez-Rios, Phys. Rev. Lett. **100**, 066408 (2008).
[23] M. Melli *et al.*, Nano Lett. **13**, 2687 (2013).
[24] S. I. Bozhevolnyi and J. Jung, Opt. Express **16**, 2676 (2008).
[25] R. Gordon, Phys. Rev. B **73**, 153405 (2006).
[26] A. Chandran, E. S. Barnard, J. S. White, and M. L. Brongersma, Phys. Rev. B **85**, 085416 (2012).
[27] P. Lalanne, J.-P. Hugonin, and J.-C. Rodier, J. Opt. Soc. Am. A **23**, 1608 (2006).
[28] C. F. Bohren and D. R. Huffman, *Absorption and Scattering of Light by Small Particles* (Wiley, Hoboken, NJ, 2008).
[29] R. G. Newton, *Scattering Theory of Waves and Particles* (Springer, New York, 1982).
[30] Z. Ruan and S. Fan, Phys. Rev. Lett. **105**, 013901 (2010).
[31] E. Palik and E. Prucha, *Handbook of Optical Constants of Solids* (Academic Press, Boston, MA, 1997).
[32] T. Søndergaard, Phys. Status Solidi B **244**, 3448 (2007).
[33] J. Jung and T. Søndergaard, Phys. Rev. B **77**, 245310 (2008).
[34] V. Siahpoush, T. Søndergaard, and J. Jung, Phys. Rev. B **85**, 075305 (2012).
[35] J. Pendry, L. Martin-Moreno, and F. Garcia-Vidal, Science **305**, 847 (2004).
[36] A. Pors, E. Moreno, L. Martin-Moreno, J. B. Pendry, and F. J. Garcia-Vidal, Phys. Rev. Lett. **108**, 223905 (2012).
[37] T. Søndergaard *et al.*, Nat. Commun. **3**, 969 (2012).
[38] M. Vasile, Z. Niu, R. Nassar, W. Zhang, and S. Liu, J. Vac. Sci. Technol. B **15**, 2350 (1997).
[39] D. De Winter and J. Mulders, J. Vac. Sci. Technol. B **25**, 2215 (2007).
[40] J.-S. Huang *et al.*, Nat. Commun. **1**, 150 (2010).
[41] H.-W. Liu *et al.*, ACS Nano **9**, 3875 (2015).
[42] A. Mooradian, Phys. Rev. Lett. **22**, 185 (1969).

[43] G. T. Boyd, Z. H. Yu, and Y. R. Shen, Phys. Rev. B **33**, 7923 (1986).
[44] M. R. Beversluis, A. Bouhelier, and L. Novotny, Phys. Rev. B **68**, 115433 (2003).
[45] P. Ghenuche, S. Cherukulappurath, T. H. Taminiau, N. F. van Hulst, and R. Quidant, Phys. Rev. Lett. **101**, 116805 (2008).
[46] A. Bouhelier, M. R. Beversluis, and L. Novotny, Appl. Phys. Lett. **83**, 5041 (2003).
[47] J. Beermann *et al.*, Opt. Express **20**, 654 (2012).
[48] J. Beermann *et al.*, New J. Phys. **15**, 073007 (2013).
[49] J. Beermann and S. I. Bozhevolnyi, Phys. Rev. B **69**, 155429 (2004).
[50] A. Pors, O. Albrektsen, I. P. Radko, and S. I. Bozhevolnyi, Sci. Rep. **3**, 2155 (2013).
[51] A. S. Roberts, A. Pors, O. Albrektsen, and S. I. Bozhevolnyi, Nano Lett. **14**, 783 (2014).
[52] S. K. Andersen, A. Pors, and S. I. Bozhevolnyi, ACS Photon. **2**, 432 (2015).
[53] V. G. Kravets, F. Schedin, and A. N. Grigorenko, Phys. Rev. Lett. **101**, 087403 (2008).
[54] B. Auguié and W. L. Barnes, Phys. Rev. Lett. **101**, 143902 (2008).
[55] A. D. Humphrey and W. L. Barnes, Phys. Rev. B **90**, 075404 (2014).
[56] A. Hohenau, J. R. Krenn, F. J. Garcia-Vidal, S. G. Rodrigo, L. Martin-Moreno, J. Beermann, and S. I. Bozhevolnyi, Phys. Rev. B **75**, 085104 (2007).
[57] J. Beermann, S. M. Novikov, T. Søndergaard, A. Boltasseva, and S. I. Bozhevolnyi, Opt. Express **16**, 17302 (2008).
[58] J. Beermann *et al.*, J. Opt. Sov. Am. B **28**, 372 (2011).
[59] S. A. Schelkunoff, Phys. Rev. **56**, 308 (1939).
[60] A. V. Lavrinenko, J. Lægsgaard, N. Gregersen, F. Schmidt, and T. Søndergaard, *Numerical Methods in Photonics* (CRC Press, Boca Raton, FL, 2014).
[61] T. Søndergaard, Y.-C. Tsao, P. K. Kristensen, T. G. Pedersen, and K. Pedersen, J. Opt. Soc. Am. B **31**, 2036 (2014).